J MATER SCI 41 (2006) 2291–2300

Mechanical properties of talc- and $CaCO_3$-reinforced high-crystallinity polypropylene composites

J.-I. WEON, H.-J. SUE*
Polymer Technology Center, Department of Mechanical Engineering, Texas A & M University, College Station, Texas 77843-3123, USA
E-mail: hjsue@tamu.edu

Published online: 3 March 2006

Toughening mechanisms and mechanical properties of two high-crystallinity polypropylene (hcPP)-based composite systems, hcPP/talc and hcPP/$CaCO_3$, are investigated. Significant improvement in tensile modulus is observed in the PP/talc composite, but only a moderate improvement is found for hcPP/$CaCO_3$. The introduction of $CaCO_3$ nanoparticles to hcPP helps nucleate a measurable amount of β-phase crystals and results in a significant drop in crystallization temperature, suggesting a possible retardation of hcPP crystallization. In addition, the hcPP/$CaCO_3$ nanocomposite shows more pronounced damping characteristics than that of hcPP/talc, throughout the temperature range studied. A detailed investigation of fracture mechanisms suggests that well-dispersed, highly oriented talc particles cause embrittlement of hcPP. Only when the crack extends toward the edges of the specimen will the crack deflection/bifurcation and microcracking mechanisms initiate. In the case of hcPP/$CaCO_3$, the $CaCO_3$ nanoparticles help trigger massive crazing and shear yielding if the testing speed is in quasi-static. The presence of β-phase crystals around the $CaCO_3$ particles could facilitate the formation of crazes throughout the hcPP matrix. Approaches for toughening hcPP are discussed.

1. Introduction

The main attraction of polypropylene (PP) is its high performance-to-cost ratio. PP can also be easily modified to achieve greatly enhanced properties. With regard to reinforcement effects, considerable research can be found in recent literature [1–13] on improving mechanical properties of PP using various kinds of inorganic fillers. It is now well recognized that the use of inorganic fillers is a useful tool for improving stiffness, toughness, hardness, chemical resistance, dimension stability, and gas barrier properties of PP [1–4]. The effects of inorganic fillers on the mechanical and physical properties of the PP composites strongly depend on the filler size, shape, aspect ratio, interfacial adhesion, surface characteristics and degree of dispersion [5–10]. Typically, the physical and mechanical properties of the polymers that contain nano-sized particles are superior to those containing micron-sized particles of the same filler type [11–13].

Talc and $CaCO_3$ are among the most commonly used fillers for PP reinforcement. $CaCO_3$ particles have an isotropic particulate structure, while talc has a plate-like structure [14]. In general, the introduction of inorganic fillers to PP leads to an increase in modulus but a decrease in toughness and ductility. However, it is well known that most semicrystalline polymers can be effectively toughened by incorporation of well-dispersed secondary phase(s) in the matrix [15–19]. Blending PP with rubber particles is an attractive way to improve toughness. However, the significant drawback of rubber toughening is loss of Young's modulus and strength, which can greatly limit its engineering applications. Therefore, there is considerable interest to simultaneously improve both the stiffness and toughness of the polymer matrix. Several studies have demonstrated an increase in both stiffness and toughness of PP and high-density polyethylene (HDPE) using rigid particles [20–29].

Bartczak *et al.* [27] used calcium stearate modified-$CaCO_3$ particles with average diameters of 3.50, 0.70 and 0.44 m to toughen HDPE. They found that the Izod impact toughness of HDPE could be improved from about

*Author to whom all correspondence should be addressed.
0022-2461
DOI: 10.1007/s10853-006-7171-x

50 J/m to 800 J/m, depending on the size and loading of $CaCO_3$ utilized. Thio *et al*. [21] reported that the introduction of micrometer-scale $CaCO_3$ particles led to an improvement in the Izod impact strength of PP by up to four times. It was found that the main toughening mechanisms were crack deflection and interfacial debonding and plastic deformation of interparticle matrix ligaments. Recently, Chan *et al*. [11] reported that the fracture toughness, termed J_{IC}, of PP increased five-fold by incorporating nanometer-scale (ca. 40 nm) $CaCO_3$ particles, and the $CaCO_3$ nanoparticles acted as stress concentrators to promote toughening mechanisms.

This study, which is part of a larger effort to improve the stiffness and toughness of high-crystallinity PP (hcPP) systems to replace glass fiber-filled PP for engineering applications, is to gain fundamental understanding on the mechanical behavior of hcPP/talc and hcPP/$CaCO_3$. It is hoped that, through this study, approaches for simultaneously improving toughness and stiffness of hcPP for structural applications can be established. A number of mechanics and microscopy techniques, such as the double-notch four-point-bending (DN-4PB) technique [23, 28–33], transmission optical microscopy (TOM), transmission electron microscopy (TEM), differential scanning calorimetry (DSC) and wide-angle X-ray diffraction (WAXD), were employed to investigate the micro-plastic deformation in the hcPP composite systems. To elucidate the dependency of strain rate on the operative toughening mechanisms in hcPP, both the *J*-integral method under a quasi-static loading condition and the Izod impact test in a dynamic loading regime were carried out. Toughening mechanisms responsible for the observed toughness improvements under both quasi-static loading and dynamic loading conditions for hcPP/talc and hcPP/$CaCO_3$ composite systems are described. Approaches for strengthening and toughening of hcPP are also discussed.

2. Experimental procedure

2.1. Sample preparation

In this study, the hcPP (BP Chemicals, Accpro® 9346), which possesses a high isotacticity and high heat resistance, has a melt flow rate of 5 g/10 min and a density of 0.906 g/cc. The two inorganic fillers chosen in this study are (1) surface-modified talc ($\rho = 2.780$ g/cc; ~2 m in size; Luzenac® R7 talc) and (2) stearic acid treated $CaCO_3$ nanoparticles ($\rho = 2.660$ g/cc; ~44 nm in size; Guang Ping Nano Technology Group Ltd).

The hcPP resin was compounded, using twin-screw extruders, with talc (11.7 vol%) and $CaCO_3$ (11.9 vol%) by Luzenac North America and Hong Kong University of Science and Technology, respectively. The mixing temperature was 180°C and the rotor speed was 60 rpm. The detailed description of the sample preparation has been documented in the literature [11]. Test specimens were injection-molded into ASTM Standard tensile and rectangular bars for mechanical testing.

2.2. DSC analysis

Non-isothermal crystallization behavior of the neat hcPP and hcPP composites was measured using Perkin-Elmer Pyris-1 DSC. All tests were executed in a nitrogen atmosphere with a sample quantity of ~10 mg. The samples were first heated from 25 to 250°C at a rate of 10°C /min. Subsequently, the samples were annealed for one minute at 250°C and then cooled to 25°C at the same rate. The melting temperature (T_m) was determined from the heating curve, while the crystallization temperature (T_c) was determined from the cooling curve.

2.3. X-ray characterization

WAXD experiments were performed at room temperature using a Bruker-AXS D8 powder diffractometer with a sealed X-ray source (Cu) in the standard vertical θ-2θ geometry (40 kV and 50 mA). A germanium incident beam monochromator was used to produce $K_{\alpha 1}$ free radiation, and a Si(Li) detector was used for data collection. The wavelength of the incident X-ray was 1.54 Å. Data were collected from 7° to 35° (2θ) at a scanning rate of 1°/min.

2.4. Mechanical property measurements

For the dynamic mechanical analysis, specimens with dimensions of 42.0 × 12.5 × 3.5 mm were cut from injection-molded tensile bars and dried under vacuum at room temperature for 24 hrs. The tests were performed under torsional mode on a Rheometric Mechanical Spectrometer (RMS-800) through a temperature range of -140 to 180 °C. The heating chamber was purged with nitrogen gas to minimize sample degradation during the test. Auto-tension and auto-strain were applied to ensure the quality of data. Measurements were made at 5°C intervals with 45 s of soaking time. The spectrometer was set to produce a sinusoidal wave function with the peak strain of 0.1%. The glass transition temperature (T_g) was assigned to be the maximum tan δ peak temperature.

Tensile properties were evaluated according to ASTM D 638. Specimens were "dog-bone" shaped and had dimensions of 63.5 × 25.4 × 5.2 mm in the gauge length region. The gripping regions at both ends were 12.7 mm wide. The tensile specimens parallel to the flow direction (FD), as shown in Fig. 1, were tested using a screw-driven mechanical testing machine (Sintech II) at a constant crosshead speed of 0.085 mm/s at room temperature. An extensometer was attached to the gage length region to measure the displacement during deformation. The Young's modulus was calculated at 0.5% strain and the yield stress was determined in accordance with the ASTM Standard. The average values and standard deviations were calculated after testing five specimens of each sample.

The *J*-integral values were obtained according to the plane strain fracture toughness standard ASTM E 813. A

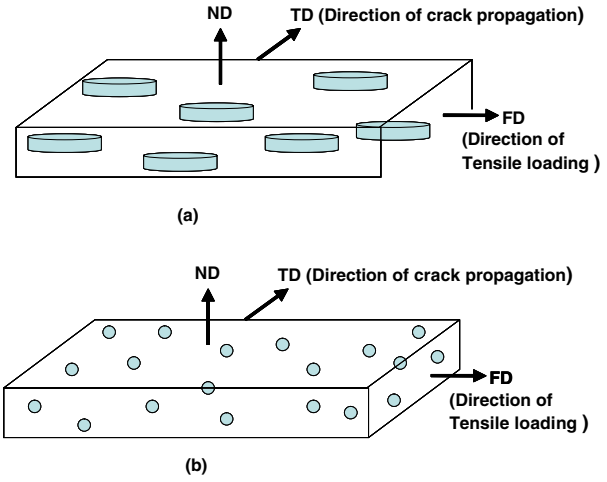

Figure 1 Schematic of dispersion of filler phases in injection molded specimens. (a) dispersed talc particles are oriented along the injection molding direction (FD) and (b) the hcPP/$CaCO_3$ nanocomposite.

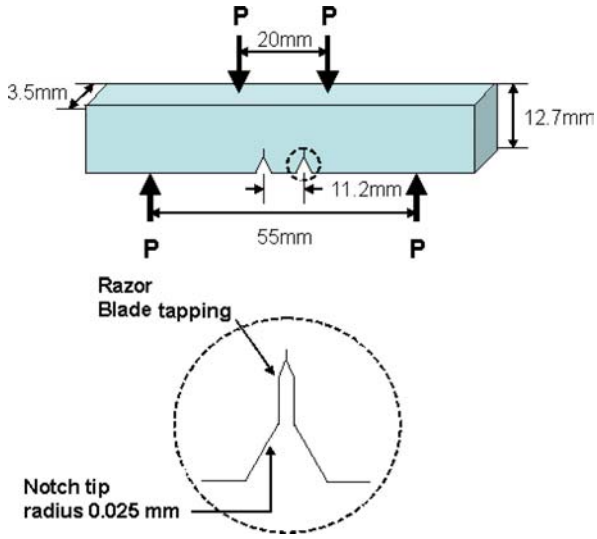

Figure 2 Details of the DN-4PB test specimen.

single-edge-notch 3-point-bend (SEN-3PB) specimen geometry was chosen for the J-integral test. The specimens had dimensions of 65.0 × 12.5 × 3.5 mm. According to ASTM E 813, the maximum load for pre-cracking should be limited to prevent the influence of plastic deformation in the case of a quasi-static fracture test. Under this load limit, the ratio of the initial crack length (a_i) to the specimen width (W), a_i/W, was controlled to be approximately 0.5 by tapping a liquid nitrogen-chilled razor blade to wedge open the initial crack. The crack propagation direction was parallel to the transverse direction (TD), as depicted in Fig. 1. A screw-driven mechanical testing machine (Instron Model 1125) was used to conduct the testing at a constant crosshead speed of 0.5 mm/min at room temperature, and the multiple specimen technique was employed for the measurement. The J_{IC} values were determined at the point of intersection between the J–R curve and the blunting line, $J = 2\sigma_y \Delta\alpha$ (where σ_y is the yield stress).

Notched Izod impact tests were conducted according to ASTM D 256 on a pendulum impact tester (Model TMI 43-02). Before the testing, the width and the depth of the specimens were measured using a micrometer. The impact strength was determined by dividing the absorbed energy by the initial cross-sectional area under the notch. Five specimens of each sample were tested and then the average values and standard deviations were calculated and reported.

2.5. Microscopy and toughening mechanism investigation

The morphology and toughening mechanisms in neat hcPP and hcPP composite systems were investigated using the DN-4PB technique [23, 28–33], TOM, and TEM. The DN-4BP samples were machined into dimension of 63.5 × 12.7 × 3.5 mm. DN-4BP bars were notched with a 250 μm radius notch cutter to a depth of 3.18 mm. The distance between two notches of DN-4BP bars was 11.2 mm. Sharp cracks were then generated by a fresh blade which had been chilled in liquid nitrogen. The details of the DN-4PB test specimen are shown in Fig. 2. The DN-4PB tests were performed using a screw-driven mechanical testing machine (Instron Model 1125). Cross-head speeds of 0.508 and 50.8 mm/min at room temperature were applied to generate sub-critical fracture of the hcPP samples. The DN-4PB Charpy impact tests were conducted on a pendulum impact tester (Model TMI 43-02) with a modified double-head striker. The DN-4-PB damage zone of the subcritically propagated crack was cut along the crack propagation direction but perpendicular to the fracture surface using a diamond saw. The plane strain core region of the crack tip damage zone was prepared for both TOM and TEM investigations.

In the TOM investigation, the damage zones were polished into thin sections with thicknesses of ~40 μm. These thin sections were observed using an Olympus BX60 optical microscope under both bright field and cross-polarization conditions to observe the overall damage zone size and features.

For the TEM experiments, the plane strain core regions of the damage zone and the intact region were carefully trimmed to an appropriate size (an area of 5 × 5 mm) and embedded in DGEBA epoxy/diethylenetriamine. The epoxy was cured at room temperature overnight. The cured block was further trimmed to about 0.3 × 0.3 mm. The trimmed block was faced off by a diamond knife and then stained with RuO_4. The faced-off block was exposed to the vapor of an aqueous RuO_4 solution (0.5% by weight) for 3 h. Ultra-thin sections, ranging from 60 to 90 nm, were obtained using a Reichert-Jung Ultracut E microtome with a diamond knife at room temperature. The thin sections were placed on 200 mesh formvar-coated copper grids and examined using a Zeiss-10C

TABLE I Summary of thermal properties of neat hcPP and hcPP composites

Sample	T_m (°C)	T_c (°C)	χ_c(%)	T_0 (°C)	t_c (min)	T_g (°C)
Neat hcPP	167	129	48.2	136	0.7	6
hcPP/talc	167	130	48.1	136	0.6	7
hcPP/$CaCO_3$	151[a], 165	121	46.7	127	0.6	8

T_m: peak meting temperature; [a]: T_m of β-crystals; T_c: peak crystallization temperature; χ_C: wt% crystallinity; T_0: onset of crystallization temperature; t_c: overall time of non-isothermal crystallization ($= |T_0 - T_C|/R$), R is the cooling rate [46]; and T_g: glass transition temperature obtained from DMA.

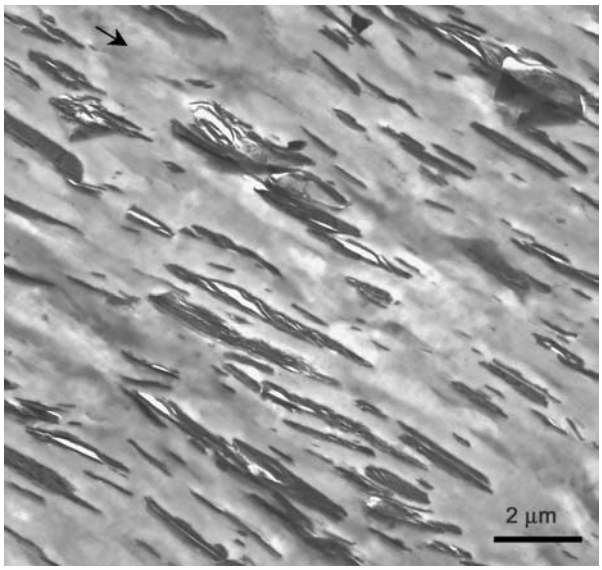

Figure 3 TEM micrograph of the hcPP/talc. The arrow indicates the flow direction.

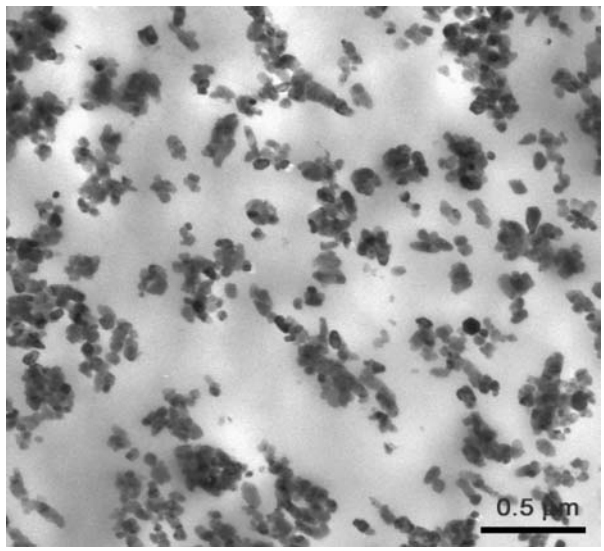

Figure 4 TEM micrograph of the hcPP/$CaCO_3$.

transmission electron microscope at an accelerating voltage of 80 kV.

3. Results and discussion

3.1. Filler dispersions in hcPP composites

Figs. 3 and 4 are TEM micrographs of the hcPP/talc and the hcPP/$CaCO_3$, respectively. It is found that the talc particles have an average aspect ratio of ∼31 and are well dispersed. In addition, the layered particles of talc are seen to be aligned along the injection-molding direction (FD), which may help contribute to good mechanical properties along the FD. On the contrary, significant amounts of aggregates are observed in the hcPP/$CaCO_3$ nanocomposite. Our earlier work [23] showed that a good dispersion could be obtained in the hcPP/$CaCO_3$ if the $CaCO_3$ loading is below 9.2 vol%. High $CaCO_3$ volume fraction may have caused the coalescence of $CaCO_3$ nanoparticles because of their high surface energy. The effect of the agglomeration of $CaCO_3$ fillers on hcPP mechanical properties will be discussed in detail later.

3.2. Crystallization of the hcPP composites

The DSC thermographs of the neat hcPP and hcPP composites are shown in Fig. 5. The weight percentage crystallinity is calculated by integrating the area under the DSC melting endothermic peak (from 120 to 200°C) and dividing by the heat of fusion with 100% crystalline PP ($\delta H_0 \approx 209\ J/g$) [19]. In the case of the hcPP composites, the heat of fusion needs to be normalized to the actual weight of hcPP. Table I gives the summary of the DSC test results. It should be noted that the addition of talc particles to the hcPP matrix did not have any significant effect on T_m, T_c, or crystallinity (χ_c). Whereas, when the $CaCO_3$ nanoparticle was dispersed in hcPP, a drop of 8°C in T_c and a slight decrease in χc were observed. Those findings are in direct contradiction to earlier work by Chan *et al.* [11], wherein the incorporation of the same size and type of $CaCO_3$ has increased T_c by 10°C for a general purpose PP. The reason for the delayed hcPP/$CaCO_3$ nanocomposite crystallization might be due to an unusual interaction between hcPP and $CaCO_3$ nanoparticles. In general, crystallization starts at chain folds to minimize the Gibbs free energy state. However, the presence of $CaCO_3$ nanoparticles in hcPP, which has a much higher isotacticity index, may have restricted chain mobility thereby inducing the formation of less-stable β-phase crystals [34, 35]. In other words, the incorporation of $CaCO_3$ nanoparticles into hcPP can decrease the T_c and χ_c by introducing a kinetic hindrance [36]. A reduction in chain mobility by kinetic hindrance results in the formation of imperfect crystallites (β-phases) and low heat of fusion, and thus, the crystal growth of hcPP is retarded [35, 37].

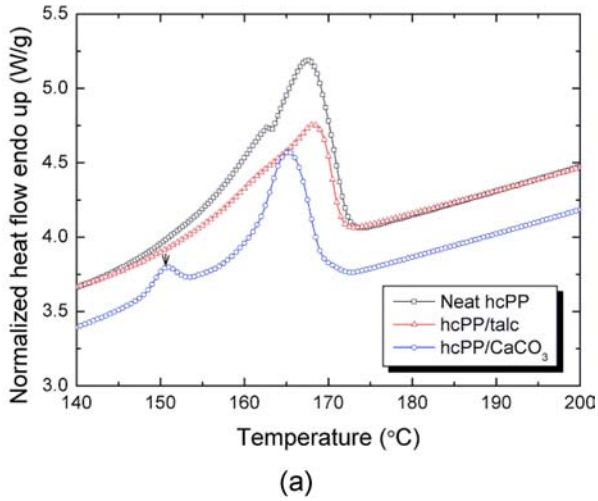

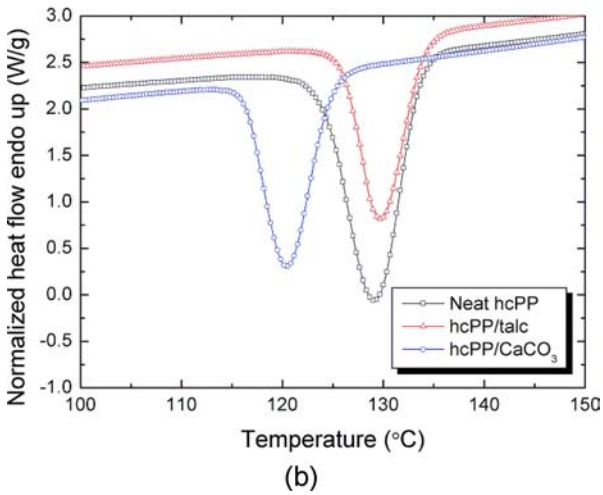

Figure 5 DSC spectra of neat hcPP and hcPP composites. (a) the melting curve and (b) the cooling curve. The arrow indicates the β-phase crystals.

To further validate the presence of the β-phase crystals in hcPP, WAXD experiments were performed. Fig. 6 shows the WAXD pattern of the neat hcPP and hcPP/$CaCO_3$ nanocomposite. Except for the strong crystallite peaks observed for α-phase crystals, a weak peak at $2\theta = 16.0^\circ$ that corresponds to the (300) crystal plan of β-phase crystals is observed. Therefore, this confirms that β-phase is formed due to the presence of $CaCO_3$ nanoparticles in the hcPP matrix. It is known that the β-phase is rarely formed unless β-nucleating agents are used [38, 39]. Zhang *et al*. [24] found that the amount of β-phase PP increases as the content of surface modifier of $CaCO_3$ particles is increased. This means that the β-phase crystals are probably formed at or near the interface of the surface-modified $CaCO_3$ particles. In other words, the $CaCO_3$ particles may be encapsulated by the β-phase crystals. If so, it may significantly affect the toughening mechanisms and the mechanical behavior of hcPP/$CaCO_3$ nanocomposite. Additional study is needed to validate this conjecture.

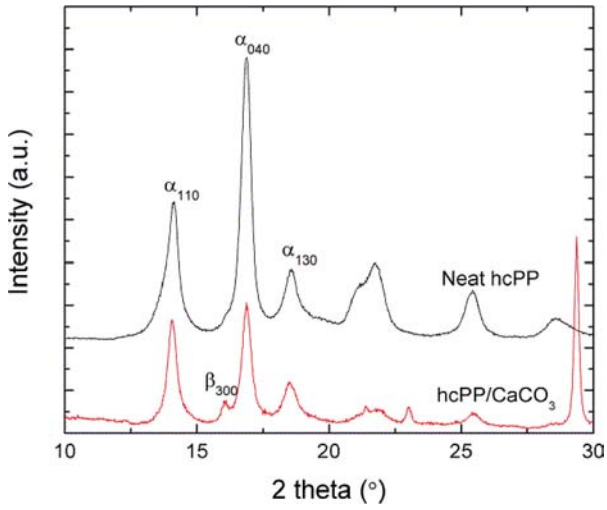

Figure 6 X-ray diffraction patterns of neat hcPP and hcPP/$CaCO_3$ composite.

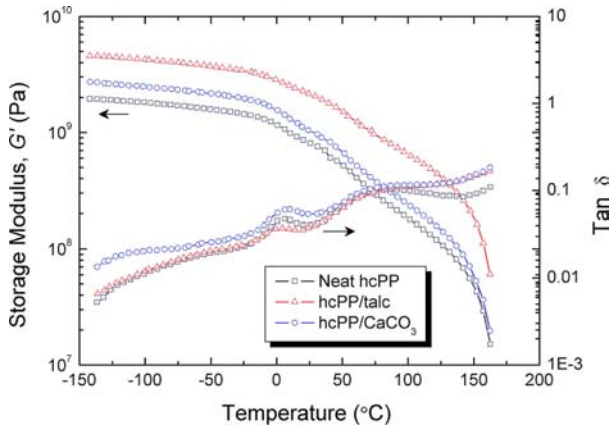

Figure 7 Dynamic mechanical spectra of neat hcPP and hcPP composites.

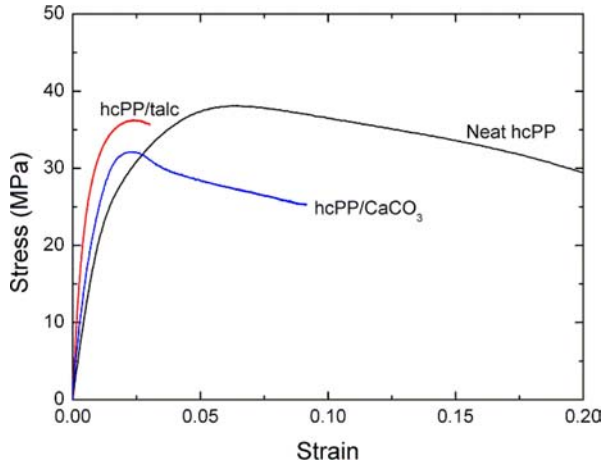

Figure 8 Typical stress-strain curves of neat hcPP and hcPP composites.

3.3. Mechanical properties

The effects of temperature on the dynamic mechanical properties of the neat hcPP and hcPP composites are shown in Fig. 7. The addition of talc and $CaCO_3$ particles into the hcPP matrix have resulted in a considerable increase in stiffness throughout the entire range of

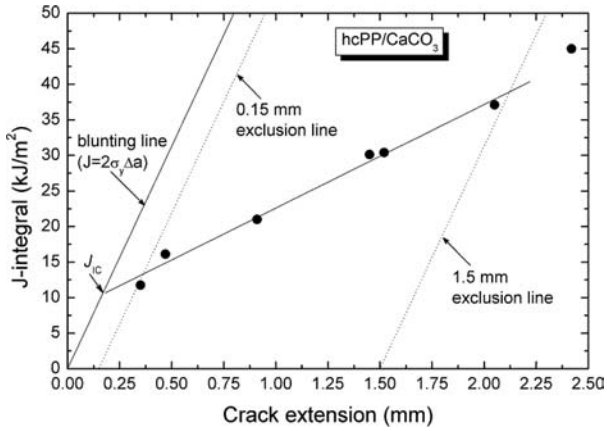

Figure 9 Representative *J-R* curves of hcPP/$CaCO_3$ composite.

TABLE II Mechanical properties of neat hcPP and hcPP composites

Sample	Elastic modulus (GPa)	Storage modulus at 25°C (GPa)	Yield stress (MPa)	Elongation at break (%)
Neat hcPP	2.10 ± 0.11	0.8	38.1 ± 0.18	290
hcPP/talc	4.31 ± 0.39	1.73	34.9 ± 0.28	4
hcPP/$CaCO_3$	2.84 ± 0.10	1.04	31.3 ± 0.75	9

TABLE III *J*-integral and Izod impact strength of neat hcPP and hcPP composites

Sample	J_{IC} (kJ/m^2)	Impact strength (kJ/m^2)
Neat hcPP	2.3	2.4 ± 0.09
hcPP/talc	1.8	2.4 ± 0.12
hcPP/$CaCO_3$	10.7	2.6 ± 0.24

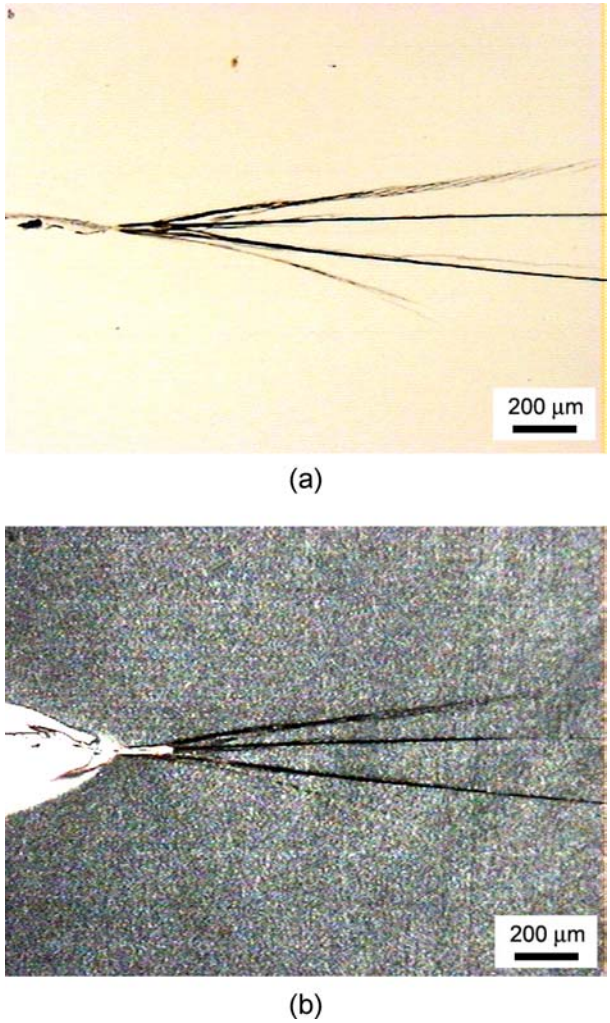

Figure 10 TOM of DN-4PB (0.508 mm/min) neat hcPP specimen taken under (a) bright field and (b) cross-polarized light. The crack propagates from left to right.

temperature scanned, as shown by the plots of storage moduli (G′) against temperature. This increase in G′ is due to the reinforcing effect of talc and $CaCO_3$ particles. It is interesting to note that the hcPP/$CaCO_3$ nanocomposite shows a higher loss tangent delta curve throughout the entire temperature range investigated. This means that the hcPP/$CaCO_3$ nanocomposite exhibits unusual molecular damping characteristics that may be due to the presence of the β-phase crystals around the $CaCO_3$ nanoparticles. These unique characteristics may have contributed to the improved toughening effects observed, as discussed below.

Typical engineering stress-strain curves are shown in Fig. 1. The neat hcPP exhibits a relatively ductile tensile drawing as compared to the hcPP composites. The key tensile properties of the hcPP and hcPP composites are reported in Table II. As expected, the hcPP composites exhibit higher Young's moduli and a slightly lower yield stress but a significant reduction in elongation at break. The hcPP/talc composite has a more significant increase in modulus than that of hcPP/$CaCO_3$ nanocomposite, due to the higher aspect ratio of talc and the talc orientation that arises from flow alignment found in the hcPP/talc composite (Fig. 3). The large increase in modulus suggests an efficient stress transfer from polymer matrix to inorganic fillers. The decrease of yield stress is likely due to the debonding between inorganic fillers and the hcPP matrix at large deformations [21]. In particular, a higher drop in yield stress is observed for hcPP/$CaCO_3$, possibly due to the splitting of aggregated particles as well as debonding between $CaCO_3$ particles and the hcPP matrix [23].

The fracture toughnesses of the neat hcPP and hcPP composites were determined in terms of the *J-R* curve and J_{IC}. The *J-R* curve with blunting lines and exclusion lines for the hcPP/$CaCO_3$ is representatively given in Fig. 9. Table III shows the J_{IC} values for the neat hcPP and the hcPP/$CaCO_3$. It is noted that the hcPP/$CaCO_3$ exhibits a significant increase in fracture toughness by about 450%. In the case of the hcPP/talc composite, the addition of talc results in a slight decrease in *J*-integral value, which is

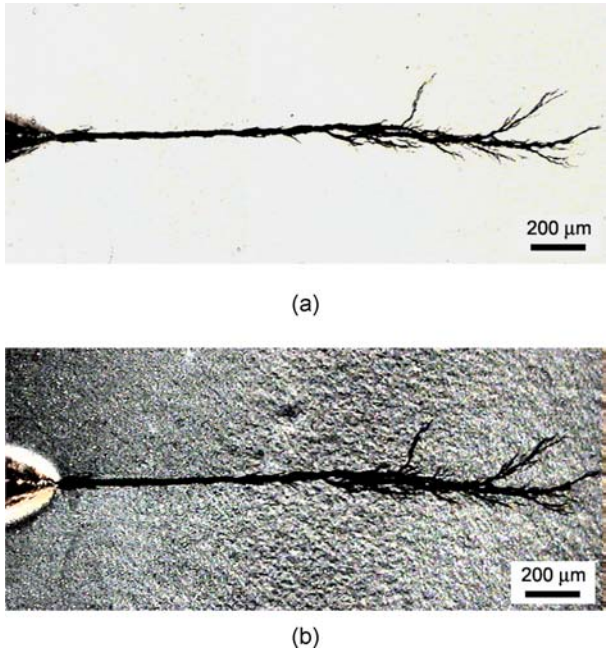

Figure 11 TOM of DN-4PB (0.508 mm/min) hcPP/talc specimen taken under (a) bright field and (b) cross-polarized light. The crack propagates from left to right.

due to the strong molecular confinement effect of talc. It should be mentioned that the hcPP/$CaCO_3$ does not break during the *J*-integral test conducted at a slow rate; one the other hand, the neat hcPP and hcPP/talc exhibit brittle unstable fracture when the crack extension is beyond 1.5 mm.

The results from the notched Izod impact strength tests, performed at room temperature, are listed in Table III. Macroscopically, all samples show signs of brittle impact fracture behavior, which shows no stress-whitening or signs of plastic deformation on the fracture surface. The addition of $CaCO_3$ particles to hcPP does not seem to improve the notched Izod impact strength. It is well known that the toughenability of polymeric materials depends on both loading rate and temperature of testing. A higher testing rate may suppress the occurrence of some toughening mechanisms, such as crazing and shear yielding, thus causing embrittlement of the polymer. The detailed investigations of the corresponding fracture mechanisms of hcPP/$CaCO_3$ under slow and fast rates are described below.

3.4. Fracture mechanism investigation

3.4.1. Toughening mechanism in neat hcPP

For comparison purposes, the toughening mechanism investigation of the neat hcPP is carried out first using TOM. Fig. 10 shows the micrographs of a DN-4PB tested specimen. As expected, the damage zone around the crack tip shows nearly featureless crack tip damage (Fig. 10); no sign of plastic deformation is observed. This fracture

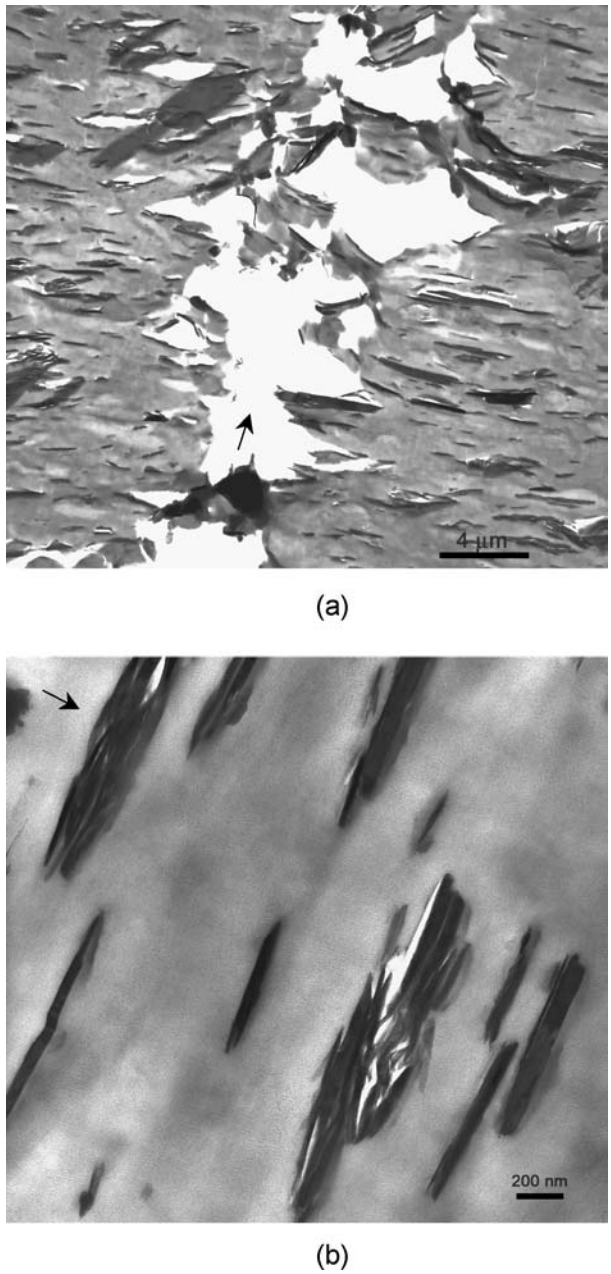

Figure 12 TEM micrographs of DN-4PB hcPP/talc composite taken (a) at the crack tip and (b) undamaged region. The arrow indicates the crack propagation direction.

mechanism corresponds well to the observed low toughness value [40, 41].

3.4.2. Toughening mechanism in hcPP/talc

TOM micrographs of the DN-4PB specimen of the hcPP/talc show crack deflection, microcracking, and bifurcation as the crack extends toward the edge of the specimen (Fig. 11a). This phenomenon may be due to the edge effect within the specimen, where a higher degree of molecular orientation as well as talc orientation is commonly observed. No sign of birefringence is observed in the crack tip damage zone under cross-polarized light

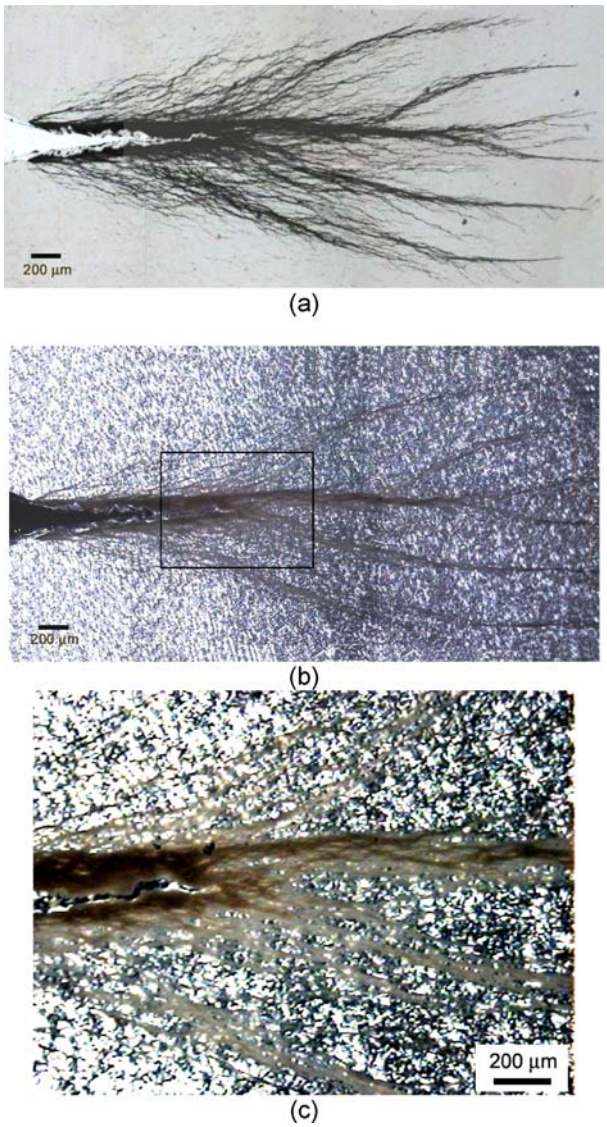

Figure 13 TOM micrographs of DN-4PB (0.508 mm/min) hcPP/$CaCO_3$ composite taken under (a) bright field, (b) cross-polarized light, and (c) a higher magnification of (b). The crack propagates from left to right.

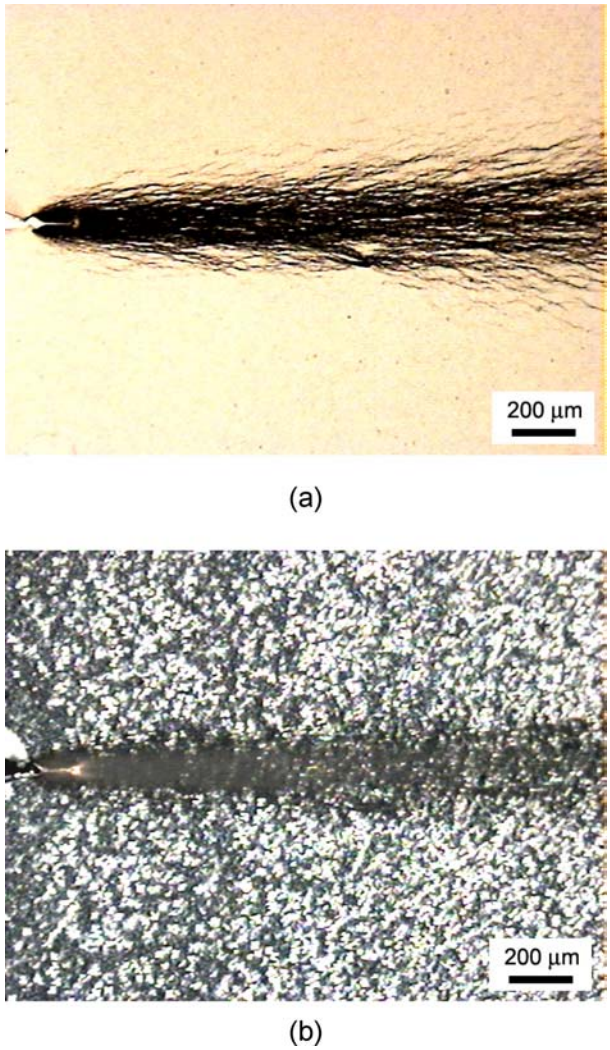

Figure 14 TOM micrographs of DN-4PB (50.8 mm/min) hcPP/$CaCO_3$ composite taken under (a) bright field and (b) cross-polarized light. The crack propagates from left to right.

(Fig. 11b). This implies that talc embrittles the hcPP matrix and leads to a lower fracture toughness. Only when the crack grows toward the highly oriented region will the less effective crack deflection, microcracking, and bifurcation mechanisms to become operative.

The TEM study performed in the sub-fracture surface zone clearly shows that the fracture behavior in hcPP/talc is in a brittle fashion (Fig. 12). Stacked layer structure of talc is found throughout the sample. Debonding between talc particles and the hcPP matrix is also observed, indicating that the interfacial bonding is weak. Talc particles appear to be effective in generating crack deflection, bifurcation, and microcracking. These fracture mechanisms are promoted due to the dispersion and orientation of talc along the injection molded direction (Fig. 3).

3.4.3. Toughening mechanism in hcPP/$CaCO_3$

The detailed toughening mechanisms of general purpose PP/$CaCO_3$ nanocomposite, which exhibit significant crazing and shear banding, has been described elsewhere [11, 23]. TOM micrographs of DN-4PB of hcPP/$CaCO_3$ nanocomposite, tested at a rate of 0.508 mm/min (slow regime), exhibit intense crazing (Fig. 13a) [7, 15, 23]. The presence of a birefringence zone under cross-polarized light indicates that shear yielding mechanisms have also occurred around the crack tip and crack wake (Figs 13b and c) [7, 15, 23]. It is noted that at slow testing speed, the toughening mechanisms observed in hcPP/$CaCO_3$ the same as those observed in general purpose PP/$CaCO_3$, but having a much smaller damage zone size.

In order to study the dependency of strain rate on fracture behavior of hcPP/$CaCO_3$ nanocomposite, additional DN-4PB tests under a testing speed of 50.8 mm/min and an impact speed of 3.4 m/s (i.e., Charpy impact test) were

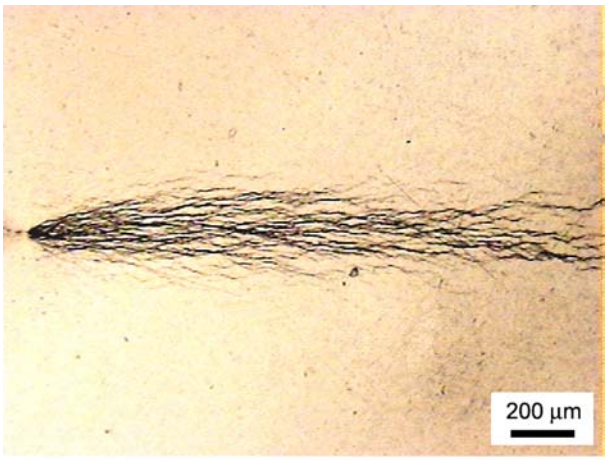

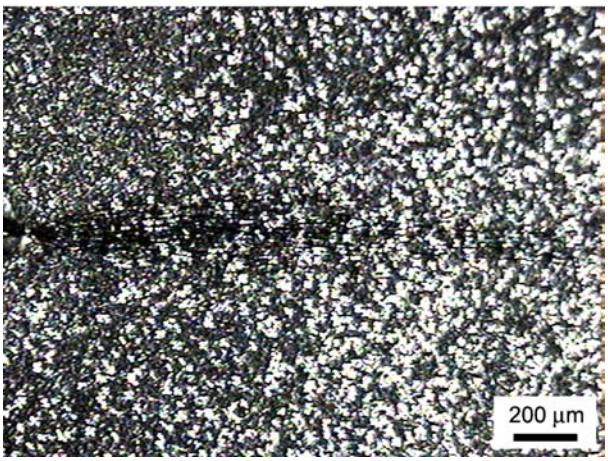

Figure 15 TOM micrographs of DN-4PB Charpy impact hcPP/$CaCO_3$ composite taken under (a) bright field and (b) cross-polarized light. The crack propagates from left to right.

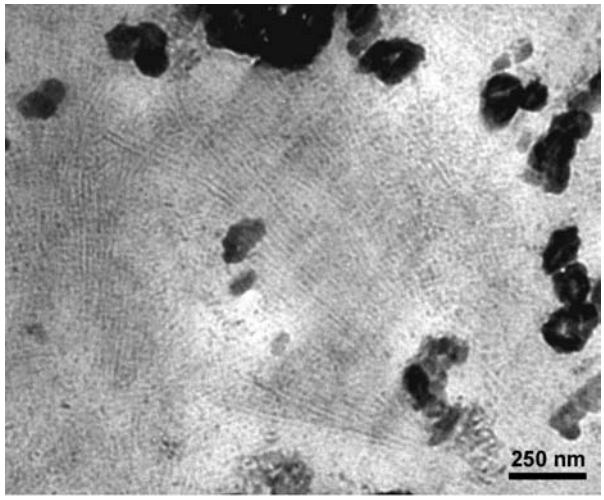

(a)

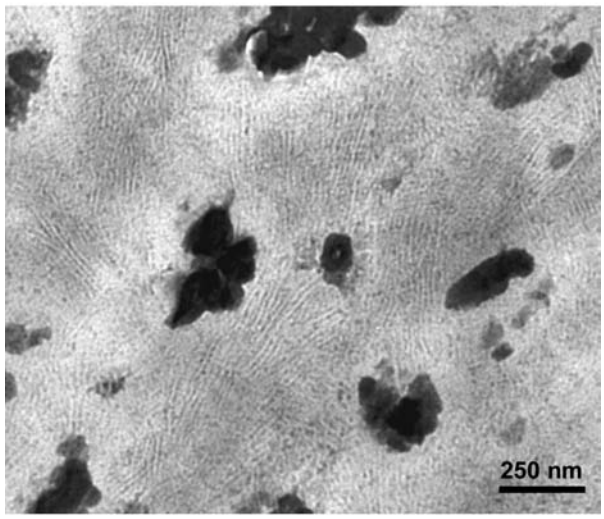

(b)

Figure 16 TEM micrographs taken from different regions showing the crystalline lamellae around the $CaCO_3$ particles of the hcPP/$CaCO_3$ composite.

performed. At a testing speed of 50.8 mm/min, it is found that a much smaller light scattering crazing zone and an accompanying birefringent zone are formed (Fig. 14). This finding is consistent with our earlier work [23], where the sequence of toughening mechanism is massive crazing, followed by shear banding of the matrix. When the DN-4PB Charpy impact test (3.4 m/s) is performed, only a small microcrack and/or crazing zone around the arrested crack tip are observed (Fig. 15a). Insignificant birefringence, if any, at the crack tip damage zone is observed (Fig. 15b). As a result, a low Izod impact strength value for the hcPP/$CaCO_3$ nanocomposite is found. The above study suggests that the fracture behavior of hcPP/$CaCO_3$ is very sensitive to testing rate.

It is interesting to note that, as shown in Fig. 16, the $CaCO_3$ nanoparticles appear to be capable of serving as nucleating agent to grow long lamellae in the hcPP matrix. These lamellae may be those of the β-phase crystals observed from the WAXS and DSC results. If true, the main reason for the effectiveness of $CaCO_3$ nanoparticles in strengthening and toughening of PP and hcPP [11, 21, 23, 24] may be its ability

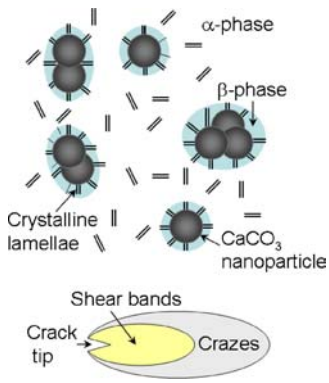

Figure 17 Schematic of the proposed morphological features of the hcPP/$CaCO_3$ composite and toughening mechanisms.

to nucleate the β-phase crystals around the $CaCO_3$ nanoparticles.

Based on the above results, the toughening process for hcPP/$CaCO_3$ is proposed. Fig. 17 illustrates a schematic of the morphological features in hcPP/$CaCO_3$. There are three key roles that the $CaCO_3$ nanoparticles have played to account for the stiffening and toughening of hcPP/$CaCO_3$ nanocomposite: (1) the high stiffness of $CaCO_3$ particles, which are responsible for modulus improvement; (2) the nucleation of β-crystals around the hcPP/$CaCO_3$ particles to increase the ductility of hcPP [42–45]; and (3) the promotion of massive crazing and the subsequent shear banding (for the slow rate testing case). Therefore, any kind of inorganic filler particles that can help nucleate the formation of β-phase crystals would potentially improve both modulus and toughness of general purpose PP and hcPP.

4. Conclusions

Strengthening and toughening mechanisms of talc and $CaCO_3$ reinforced hcPP-based composites have been examined. The high aspect ratio and high degree of orientation of talc along the tensile direction are responsible for the observed dramatic improvement in modulus. The fracture toughness of hcPP is significantly affected by the addition of $CaCO_3$ at slow testing speeds. It is believed that $CaCO_3$ nanoparticles act as effective nucleation sites to trigger massive crazing and shear yielding in the hcPP matrix. Our results suggest that the incorporation of $CaCO_3$ nanoparticles into hcPP can produce attractive polymer nanocomposite with improved modulus and toughness.

Acknowledgments

The authors would like to thank BP Chemical for donating the hcPP resin and Luzenac North America for providing talc and performing compounding and injection molding of the samples. Special thanks are also given to Defense Logistic Agency (SP0103-02-D-0024) and State of Texas ARP Grant (000512-00137-2001) for their financial support. Research collaboration with Professor C.-M. Chan of the Hong Kong University of Science and Technology is acknowledged.

References

1. A. TABTIANG and R. VENABLES, *Eur. Polym. J.* **36** (2000) 137.
2. C. A. WAH, L. CHOONG and G. S. NEON, *ibid.* **36** (2000) 789.
3. K. PREMPHET and P. HORANOT, *Polymer* **41** (2000) 9283.
4. Z. BARTCZAK, A. S. ARGON, R. E. COHEN and M. WEINBERG, *Polymer* **40** (1999) 2347.
5. J. Z. LIANG and R. K. Y. LI, *J. Appl. Polym. Sci.* **77** (2000) 409.
6. K. MITSUISHI, S. KODAMA and H. KAWASAKI, *Polym. Engng. Sci.* **25** (1985)1069.
7. G.-X. WEI and H.-J. SUE, *J. Mat. Sci.* **35** (2000) 555.
8. J. JANCAR and A.T. DIBENEDETTO, *Polym. Engng. Sci.* **33** (1993) 559.
9. Z. DEMJEN, B. PUKANSZKY and N. JOZSEF, *Composites Part A* **29** (1998) 323.
10. R. ROTHON, in "Particulate-Filled Polymer Composites" (Wiley, New York, NY, 1995).
11. C. CHAN, J. WU, J. LI and Y. CHEUNG, *Polymer* **43** (2002) 2981.
12. M. SUMITA, T. SHIZUMA, K. MIYASAKA and K. ISHIKAWA, *J. Macromol. Sci. Phys.* **B22** (1983) 601.
13. M. SUMITA, T. TSUKURMO, K. MIYASAKA and K. ISHIKAWA, *J. Mater. Sci.* **18** (1983) 1758.
14. M. FUJIYAMA and T. WAKINO, *J. Appl. Polym. Sci.* **42** (1991) 2749.
15. G.-X. WEI, H.-J. SUE, J. CHU, C. HUANG and K. GONG, *J. Mater. Sci.* **35** (2000) 555.
16. H.-J. SUE, *J. Mater. Sci.* **27** (1992) 3098.
17. G.-X. WEI and H.-J. SUE, *Polym. Eng. Sci.* **40** (2000) 1979.
18. Y. LI, G.-X. WEI and H.-J. SUE, *J. Mater. Sci.* **37** (2002) 2447.
19. G.-X. WEI, H.-J. SUE, J. CHU, C. HUANG and K. GONG, *Polymer* **41** (2000) 2947.
20. Z. BARTCTCZAK, *J. Macromol. Sci. Part B: Phys.* **B41** (2002) 1205.
21. Y. S. THIO, A. S. ARGON, R. E. COHEN and M. WEINBERG, *Polymer* **43** (2002) 3661.
22. W. C. J. GAYMANS, C. WESTZAAN, J. HUETINK and R. J. GAYMANS, *ibid.* **44** (2003) 261.
23. J.-I. WEON, K. T. GAM, W. J. BOO, H.-J. SUE and C.-M. CHAN, *J. Appl. Polym. Sci.* accepted.
24. Q. X. ZHANG, Z. Z. YU, X. L. XIEA and Y. W. MAI, *Polymer* **45** (2004) 5985.
25. A. S. ARGON and R. E. COHEN, *Polymer* **44** (2003) 6013.
26. Q. FU and G. H. WANG, *Polym. Eng. Sci.* **32** (1992) 94.
27. Z. BARTCZAK, A. S. ARGON, R. E. COHEN and M. WEINBERG, *Polymer* **40** (1999) 2331.
28. H.-J. SUE and A. F. YEE, *J. Mater. Sci.* **28** (1993) 2915.
29. H.-J. SUE, *Polym. Eng. Sci.* **31** (1991) 270.
30. H.-J. SUE and A. F. YEE, *J. Mater. Sci.* **24** (1989) 1447.
31. J. LU, G.-X. WEI, H.-J. SUE and J. CHU, *J. Appl. Polym. Sci.* **76** (2000) 311.
32. J. LU, C. K. Y. LI, G.-X. WEI and H.-J. SUE, *J. Mater. Sci.* **35** (2000) 271.
33. G.-X. WEI and H.-J. SUE, *J. Appl. Polym. Sci.* **74** (1999) 2539.
34. W. C. J. ZUIDERDUIN, C. WESTZAAN, J. HUETINK and R. J. GAYMANS, *Polymer* **44** (2003) 261.
35. T. KOWALESKI and A. GALESKI, *J. Appl. Polym. Sci.* **32** (1986) 2919.
36. R. GRECO and F. COPPOLA, *Plast. Rubber. Process. Appl.* **6** (1986) 35.
37. F. H. J. MAURER, H. M. SCHOFFELEERS, R. KOSFELD and T. UHLENBROICH, Progress in Science and Engineering of Composites. Tokyo: ICCM-IV; 1982, p. 803.
38. J. J. LIU, X. F. WEI and Q. P. GUO, *J. Appl. Polym. Sci.* **41** (1990) 2829.
39. P. M. MCGENITY, J. J. HOOPER, C. D. PAYNTER, A. M. RILEY, C. NUTBEEM, N. J. ELTON and J. M. ADAMS, *Polymer* **33** (1992) 5215.
40. R. GRECO and G.RAGOSTA, *J. Mater. Sci.* **23** (1988) 4171.
41. H. G. OLF and A. PETERLIN, *J. Polym. Sci. Polym. Phys.* **12** (1974) 2209.
42. S. C. TJONG, J. S. SHEN and R. K. Y. LI, *Polymer* **37** (1996) 2309.
43. S. C. TJONG, R. K. Y. LI and T. CHEUNG, *Polym. Eng. Sci.* **37** (1997) 166.
44. T. LABOUR, G. VIGIER, R. SEGUELA, C. GAUTHIER, G. ORANGE and Y. BOMAL, *J. Polym. Sci. Part B: Polym. Phys.* **40** (2002) 31.
45. T. LABOUR, L. FERRY, C. GAUTHIER, P. HAJJI and G. VIGIER, *J. Appl. Polym. Sci.* **74** (1999) 195.
46. Z. WU, C. ZHOU and N. ZHU, *Poly. Test.* **21** (2002) 479.

Received 6 April
and accepted 28 June 2005